Xu *et al. Microstructures* 2023;3:2023034
DOI: 10.20517/microstructures.2023.19

Microstructures

Research Article

Open Access

Check for updates

Optimizing the energy storage performance of $NaNbO_3$ ceramics by rare-earth-based composite perovskite $Sm(Mg_{0.5}Zr_{0.5})O_3$ modification

Mingzhao Xu, Dafu Zeng, Xiang Wang, Peng Nong, Yue Pan, Qinpeng Dong, Jiaming Wang, Huanfu Zhou, Xiuli Chen

Key Laboratory of Nonferrous Materials and New Processing Technology, Ministry of Education, School of Materials Science and Engineering, Guilin University of Technology, Guilin 541004, Guangxi, China.

Correspondence to: Prof. Huanfu Zhou, Key Laboratory of Nonferrous Materials and New Processing Technology, Ministry of Education, School of Materials Science and Engineering, Guilin University of Technology, Guilin 541004, Guangxi, China. E-mail: zhouhuanfu@163.com; Prof. Xiuli Chen, Key Laboratory of Nonferrous Materials and New Processing Technology, Ministry of Education, School of Materials Science and Engineering, Guilin University of Technology, Guilin 541004, Guangxi, China. E-mail: cxlnwpu@163.com

How to cite this article: Xu M, Zeng D, Wang X, Nong P, Pan Y, Dong Q, Wang J, Zhou H, Chen X. Optimizing the energy storage performance of $NaNbO_3$ ceramics by rare-earth-based composite perovskite $Sm(Mg_{0.5}Zr_{0.5})O_3$ modification. *Microstructures* 2023;3:2023034. https://dx.doi.org/10.20517/microstructures.2023.19

Received: 20 Apr 2023 **First Decision:** 13 Jul 2023 **Revised:** 9 Aug 2023 **Accepted:** 17 Aug 2023 **Published:** 1 Sep 2023

Academic Editor: Shujun Zhang **Copy Editor:** Fangyuan Liu **Production Editor:** Fangyuan Liu

Abstract

Researchers often improve the energy storage performance of $NaNbO_3$ ceramics through doping with Bi-based composites. Recent studies have shown that rare-earth elements, such as La and Sm, can suppress remanent polarization. In this study, a $(1-x)NaNbO_{3-x}Sm(Mg_{0.5}Zr_{0.5})O_3$ ceramic system was designed. Doping with $Sm(Mg_{0.5}Zr_{0.5})O_3$ (SMZ) increases the resistance, activation energy, and bandgap of $NaNbO_3$ ceramics, improves the breakdown field strength, and optimizes the energy storage efficiency of $NaNbO_3$ ceramics. In this study, $0.92NaNbO_3$-0.08 SMZ achieved an energy storage density of 4.3/cm^3 and an energy storage efficiency of 85.6% at 560 kV/cm. When x = 0.15, the sample exhibited an ultrahigh breakdown field strength and energy storage efficiency (720 kV/cm and 91%, respectively). In addition, the 0.08 SMZ sample had an ultrafast release rate of $t_{0.9}$ (57 ns), high current density (777.1 A/cm^2), and high power density (69.93 MW/cm^3). It has practical application prospects in high-performance energy storage capacitors.

Keywords: $NaNbO_3$, energy storage density, rare-earth modification

INTRODUCTION

$NaNbO_3$-based energy storage dielectric ceramics have excellent electrical properties, such as antiferroelectric (AFE) properties, high polarization strength, and relative breakdown resistance. They are lightweight and have a wide working temperature range, which is beneficial for practical applications and has attracted the attention of many researchers[1,2]. By using $NaNbO_3$ as the base and adding a variety of structural compounds to form solid solutions with different properties, energy storage dielectric ceramics with excellent performance can be obtained[3,4]. However, as an AFE material, $NaNbO_3$ decreases the energy storage efficiency owing to the large polarization hysteresis caused by the inevitable field-induced AFE-relaxor ferroelectric (FE) phase transition while obtaining a high energy density[5,6].

Researchers often adjust the relaxation behavior of ceramics, reduce the average grain size, stabilize the AFE type, and delay the AFE-FE transition by incorporating doping Bi-based composite perovskites to improve the energy storage performance of $NaNbO_3$-based ceramics. For instance, $NaNbO_3$ doped with $Bi(Ni_{0.5}Zr_{0.5})O_3$ exhibits a breakdown field strength of 500 kV/cm, an energy storage density of 4.90 kV/cm^3, and an efficiency of 73%[7]. An energy storage density of 3.70 J/cm^3 and an energy storage efficiency of 77% were obtained through doping with $Bi(Mg_{2/3}Nb_{1/3})O_3$ ceramics with a breakdown field strength of 460 kV/cm[1]. Good results have been achieved, but the challenge of achieving low energy storage efficiencies persists. Notably, there is still a lack of research on rare-earth-based composite perovskites.

Ye studied $0.96Na_{0.88}La_{0.12}NbO_3$-$0.04CaSnO_3$[8], and a 2.1 /cm^3 recoverable energy storage density (W_{rec}) and 62% energy storage efficiency (η) were obtained. Although the energy storage performance was general, doping with La inhibited P_r. The ceramics doped with $La(Mg_{0.5}Zr_{0.5})O_3$ in a $Sr_{0.7}Bi_{0.2}TiO_3$ matrix studied by Chen achieved an energy storage density of 1.22 J/cm^3 and an ultrahigh energy storage efficiency of 98.2%[9]. The energy storage density was low, but η was high. Yang[10] obtained a 6.5 J/cm^3 W_{rec} and 96% η by adding Sm^{3+} and Ti^{4+} to $NaNbO_3$. This shows that the energy storage efficiency of the matrix can be changed by doping with rare-earth elements.

In studies of $NaNbO_3$, $BaTiO_3$, and $Sr_{0.7}Bi_{0.2}TiO_3$ ceramics, doping with Bi $(Mg_{0.5}Zr_{0.5})O_3$ helped maintain good performance stability[9,11,12]. Based on the above research, $Sm(Mg_{0.5}Zr_{0.5})O_3$ (SMZ) was introduced into a $NaNbO_3$ matrix, and $(1-x)NaNbO_3$-$xSm(Mg_{0.5}Zr_{0.5})O_3$ (x = 0.05, 0.08, 0.12, and 0.15) (NN-SMZ) ceramics were designed. The electrical properties, such as energy storage performance, temperature stability, frequency stability, and resistance, were analyzed and studied. It is concluded that the energy storage performance of the matrix can be improved by doping Sm^{3+} ions at the A site of the perovskite structure, and the performance stability of the ceramics can be improved.

EXPERIMENTAL PROCEDURE

NN-SMZ was prepared using a conventional solid-state reaction. Na_2CO_3 (99.8%), Nb_2O_5 (99%), Sm_2O_3 (99.99%), ZrO_2 (99%), and MgO (98.5%) were stoichiometrically weighed and ball-milled with Zr balls in ethanol for 5 h. After drying, the mixed powders were calcined at 900 °C for 5 h and ball-milled again for 5 h. Polyvinyl alcohol (5%) was added as a binder to press the dried powder into a disk with a diameter of 8 mm and thickness of 1 mm. The disks were calcined at 550 °C for 4 h for glue extrusion. Finally, the samples were embedded in a precursor powder of the same composition and sintered at 1,340 °C for 2 h. The test instrument information during the experiment is added to the support material. The thicknesses and silver electrode areas of the samples used for P-E testing are listed in Supplementary Table 1.

RESULTS AND DISCUSSION

The X-Ray diffraction analysis (XRD) patterns of the NN-SMZ ceramics are shown in Figure 1A. Enlarging the characteristic peak clearly shows that with the addition of SMZ, the (200) characteristic peak shifts to a lower angle, indicating that the sample lattice has expanded[13,14]. After doping with SMZ, Sm^{3+}(1.24 Å) partially replaces Na^{+} (1.39 Å) at the A site, and Mg^{2+} (0.72 Å) and Zr^{4+} (0.72 Å) replace the smaller Nb^{5+} (0.64 Å) at the B site[15]. The results show that the lattice expansion of the sample was mainly affected by the introduction of Mg^{2+} and Zr^{4+} at the B site[7]. To explore the reason for this phenomenon, the NN-SMZ component samples were refined. The refined results are shown in Figure 1B-E and Supplementary Figure 1. The $NaNbO_3$ ceramic exhibited an orthorhombic phase at room temperature; with the increase in SMZ doping, the sample gradually changed from the orthorhombic phase (*Pnma*) to the pseudocubic phase (*Pm3m*). When x = 0.05 and 0.08, the sample exhibited a two-phase coexistence phenomenon. Supplementary Figure 2 shows the refinement results for the NN-SMZ at 35°-45°. The refinement result for the sample was good. As the sample gradually changed to the pseudocubic phase, the intensity of the superlattice diffraction peak gradually decreased.

The Raman spectra of each component sample are shown in Figure 2A. The gradually widened peak width and gradually decreased peak intensity indicate that the complexity of the sample and the disorder of ions increased owing to the nonequivalent substitution of ions with different radii at the A and B sites[16,17]. To study further the effect of adding SMZ to the system, Peakfit software was used to analyze the Raman spectra of each component sample. The center position, peak intensity, and peak half-width of the vibration modes ν_1 and ν_5 fitted by each Raman component are shown in Figure 2B and C. With an increase in the SMZ content, the peak intensities of vibration modes ν_1 and ν_5 gradually decreased, and the half-width and height gradually increased, which proved that the complexity of the sample and the disorder of the ions increased. The vibration mode ν_5 moved to a high-wavenumber position, and a blue shift occurred. The red shift of the vibration mode ν_1 may be caused by the phase transition of the sample, which corresponds to the XRD refinement results in this study[18].

Scanning electron microscopy (SEM) images of the NN-SMZ components under the natural surface and the average grain size fitted by the Gaussian function are shown in Figure 3A. The surfaces of the NN-SMZ ceramic component samples were dense and had no obvious defects, and the average grain size generally increased. The grain sizes of 0.08 SMZ and 0.12 SMZ significantly increased. According to the XRD refinement results, the appearance of the pseudo-cubic phase is one reason for this phenomenon. According to the formula $E_b \propto G^{-1/2}$, the grain size (G) is negatively correlated with the breakdown field strength (E_b). The grain size of each component is smaller than that of pure $NaNbO_3$ (generally tens of micrometers)[19,20], which helps the samples obtain a higher E_b[21]. The energy dispersive spectrometry (EDS) mapping of the 0.08 SMZ ceramic is shown in Figure 3B. Each element was uniformly distributed without enrichment, indicating that the SMZ was uniformly dissolved in the NN lattice[22]. An atomic force microscopy analysis was performed on the samples after hot corrosion. The test results are shown in Supplementary Figure 3. The surface of each component sample was dense, without obvious pores or defects. The sintering densities of the NN-SMZ samples are shown in Supplementary Table 2. The incorporation of the SMZ reduced the sintering temperature, improved the density of the ceramics, and helped the samples obtain a higher breakdown field strength.

A Transmission Electron Microscope test can effectively observe the domain morphology and phase structure of FE materials. The domain morphology of pure $NaNbO_3$ ceramics is shown in Figure 4A and clearly shows the existence of a 180° domain. The domain morphology of the 0.08 SMZ sample is shown in Figure 4B, and the larger domain cannot be clearly observed, which is related to the gradual transition of the

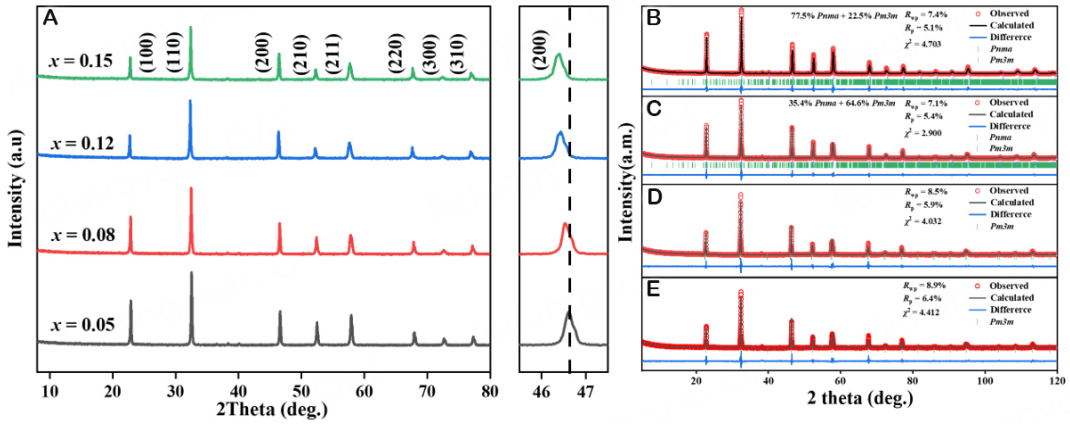

Figure 1. XRD patterns of $NaNbO_{3-x}Sm(Mg_{0.5}Zr_{0.5})O_3$ ceramics ($0.05 \leq x \leq 0.15$) (A), (B) XRD refinement of 0.05 SMZ component, (C) XRD refinement of 0.08 SMZ component, (D) XRD refinement of 0.12 SMZ component, and (E) XRD refinement of 0.15 SMZ component.

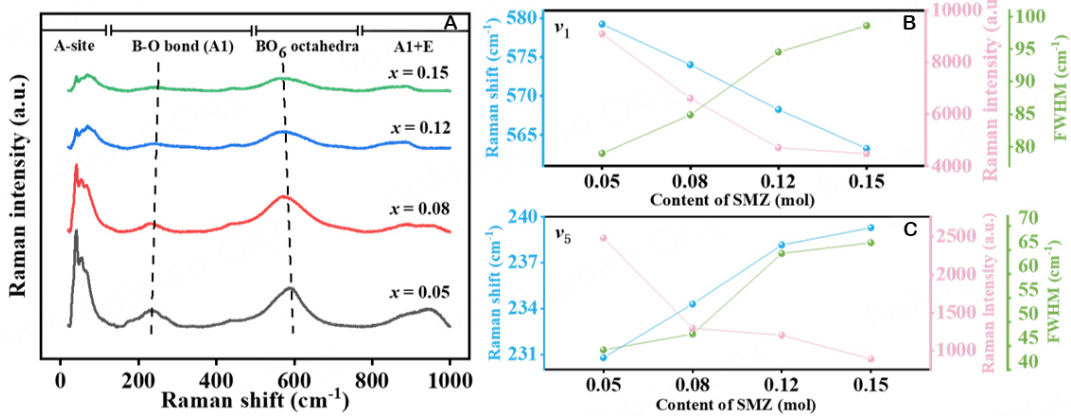

Figure 2. Raman Test Diagram of $NaNbO_{3-x}Sm(Mg_{0.5}Zr_{0.5})O_3$ ceramics ($0.05 \leq x \leq 0.15$) (A) and the Raman vibration modes v_1 (B) and v_5 (C) of NN-SMZ components are plotted.

phase structure of the sample to the weak polar pseudocubic phase[23]. In $NaNbO_3$ ceramics, due to the presence of large-sized domains, when the polarization direction changes, the direction of the domain will be irreversible, which greatly deteriorates the energy storage performance of the ceramics. The domain sizes of the 0.08 SMZ ceramic sample were smaller, which was beneficial to the sample to obtain a faster polarization response in the charge and discharge test, reduced the polarization loss, and achieved the purpose of improving the energy storage performance of the sample[24]. Figure 4C and D depicts selected area electron diffraction (SAED) images of 0.08 SMZ samples taken in the $[100]_c$ and $[111]_c$ directions. The presence of (eoo)/2 and (oee)/2 in the $[100]_c$ direction and the presence of (ooe)/2 superlattice diffraction spots in the $[111]_c$ direction (o and e are odd and even, respectively) proved the existence of octahedral distortion, indicating that this was a commensurate modulation phase structure with two-fold unit cell. The SEAD images also proved the perovskite structure of the 0.08 SMZ sample again[25].

To investigate the change in the dielectric constant of NN-SMZ ceramics with temperature, the dielectric constant of NN-SMZ was tested at -160 °C to 180 °C. The temperature spectra of the components are shown in Figure 5A-D, where the dielectric peaks of the components near 0 °C formed because of the

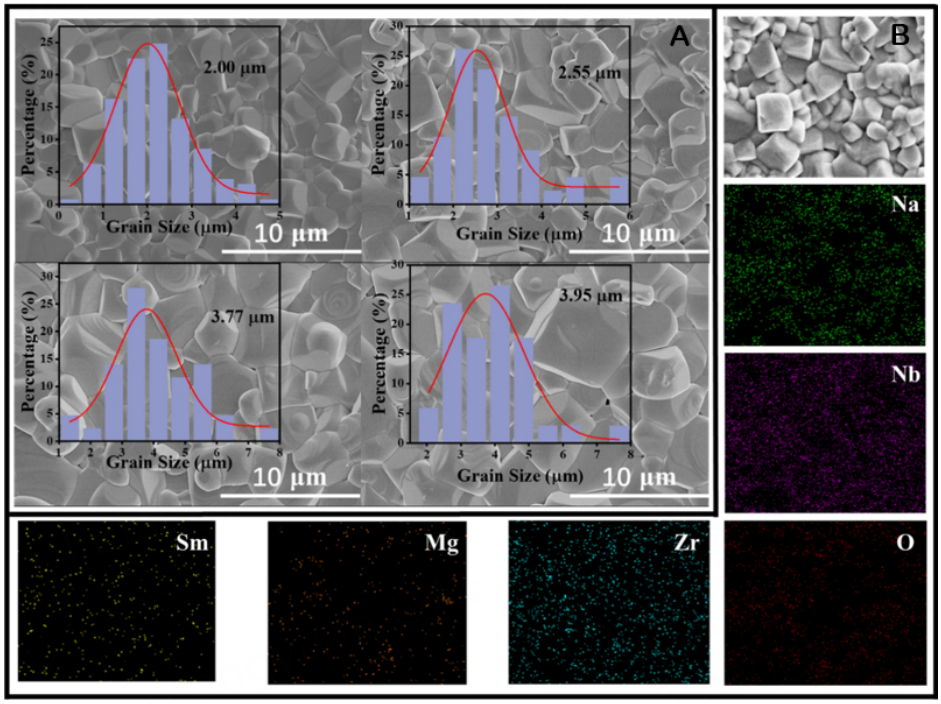

Figure 3. SEM images (A) and EDS mapping images of the NN-SMZ ceramic (B).

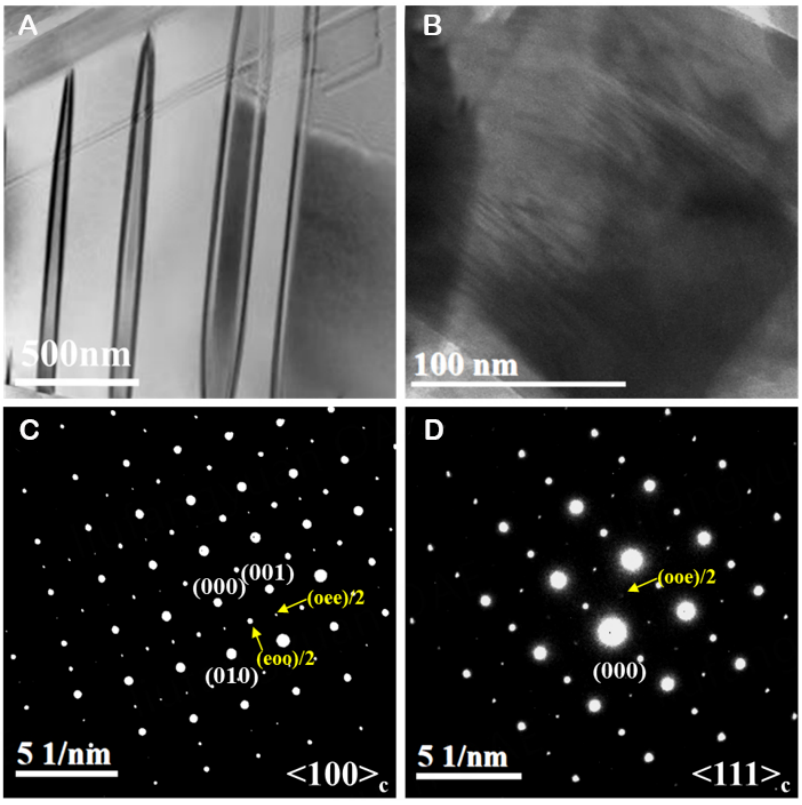

Figure 4. (A) Domain morphology of NN ceramics, (B) domain morphology of 0.08 SMZ ceramics. Lattice fringes and SAED patterns of 0.92 NN-0.08 SMZ ceramics along (C) $[100]_c$ and (D) $[111]_c$.

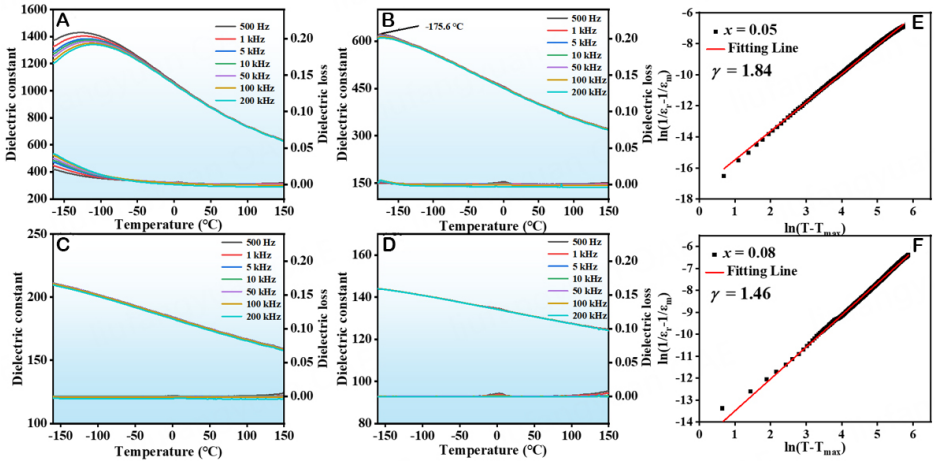

Figure 5. Temperature dependences of dielectric constant and loss of NN-SMZ ceramics: (A) x = 0.05, (B) x = 0.08, (C) x = 0.12, (D) x = 0.15. Fitting analysis of ln(1/εr-1/εm) *versus* ln(T-Tm) for NN-SMZ ceramics at 500 kHz: (E) x = 0.05, (F) x = 0.08.

interference of ice during the temperature change. They are not phase transition peaks[26]. The figure shows that the 0.05 SMZ sample had an obvious dielectric peak; the Curie temperature was near -120 °C, and the dielectric peak of the 0.08 SMZ sample appeared at -175.6 °C. The dielectric peaks of the 0.12 SMZ and 0.15 SMZ samples were not obtained in the test. This may have resulted from the addition of SMZ, which caused the dielectric peak of the sample to shift to a lower temperature. The Curie temperature of the 0.12 SMZ and 0.15 SMZ samples was lower than the test temperature. As the amount of SMZ doping increased, the dielectric peak of the material gradually disappeared. The T-ε_r curve of the material gradually becomes a flattened, somewhat straight line, showing the dielectric temperature spectrum characteristics of the linear dielectric material[27].

The dispersion coefficients of 0.05 SMZ and 0.08 SMZ samples fitted according to the dielectric peak are shown in Figure 5E and F. The increase in the SMZ content reduces the dispersion coefficient of the sample. This means that the relaxation and the polar microregion of the sample are reduced, which is consistent with the Raman and XRD results. The frequency stability of the dielectric constant of the NN-SMZ ceramics is shown in Supplementary Figure 4. The samples of each component can maintain the stability of the dielectric constant over a wide frequency range of 10^3-10^6[28].

The P-E curve obtained by the FE test of the sample provides direct evidence for evaluating the energy storage performance of the sample, and the relevant energy storage performance calculation formula is provided in the supporting materials[6]. The test results for the NN-SMZ component samples at a field strength of 400 kV/cm are shown in Figure 6A-C. With an increase in x, the maximum polarization intensity P_{max} of the sample decreased, the residual polarization intensity P_r decreased, and the obtained energy storage efficiency increased from 71.1% to 93.1%. This is because, with the incorporation of SMZ, the phase of the NN-SMZ sample gradually transformed into a weakly polar pseudocubic phase, which reduced the P_{max} and P_r of the sample, leading to the gradual reduction of domains in the sample[23]. The results are consistent with the results of the Raman test and dielectric-constant-frequency test, proving that the doping of rare-earth-based composite perovskites can significantly increase the energy storage efficiency of the sample. Figure 6D-F shows the maximum breakdown field strength FE test diagrams of the component samples of NN-SMZ. As the figure shows, the breakdown field strength of the sample increased with the increase in the ratio. When x = 0.08, the sample exhibited the best energy storage performance. The breakdown field strength of the sample was 560 kV/cm, the energy storage density was 4.3 J/cm^3, and the

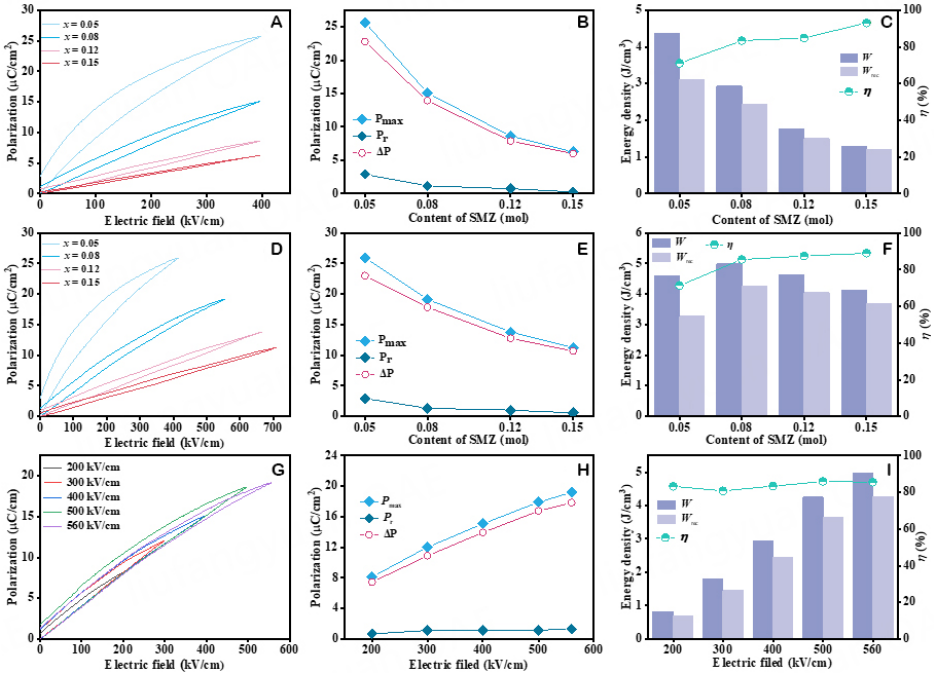

Figure 6. For NN-SMZ ceramics: at the electric field of 400 kV/cm: Unipolar P-E hysteresis loops (A), the corresponding energy storage properties (B) and polarization (C) at various content of SMZ. Unipolar P-E hysteresis loops (D), the corresponding energy storage properties (E), and polarization (F) at all content of SMZ. 0.08 SMZ unipolar P-E hysteresis loops (G), the corresponding energy storage properties (H) and polarization (I) at 0.08 SMZ.

energy storage efficiency was 85.6%. When x = 0.15, the breakdown field strength of the sample reached 720 kV/cm, indicating that the addition of SMZ significantly improved the E_b of the sample. Figure 6G-I shows the FE test results for the 0.08 SMZ samples under different field strengths. With an increase in the field strength, the P_{max} of the sample increased, and the number of domains that could not be flipped increased, resulting in an increase in P_r. In summary, the addition of the SMZ increased the energy storage efficiency and breakdown field strength of the samples[29].

The frequency stability of the *P-E* curve of the 0.08 SMZ ceramics is shown in Figure 7A-C. At an electric field of 350 kV/cm and different frequencies, the 0.08 SMZ ceramics exhibited a stable energy storage density of 1.9 ± 0.02 J/cm³ and a stable energy storage efficiency. This shows that 0.08 SMZ ceramics have excellent frequency stability and practical application prospects[30,31]. The temperature stability of the 0.08 SMZ ceramics is shown in Figure 7D-F. At a frequency of 10 Hz and an electric field of 350 kV/cm, the energy storage performance of the sample decreased with increasing temperature. The P_{max} and P_r of the samples increased with an increase in temperature, which may have been caused by the deterioration of the leakage current and boosted mobility of the domain walls at high temperatures[23].

To study the intrinsic mechanism of high E_b in NN-SMZ ceramics, we discussed the non-intrinsic factors and intrinsic factors with the sample[31]. We used the phase field method to simulate the electrical breakdown behavior of pure $NaNbO_3$ ceramics and 0.08 SMZ ceramic samples. The initial geometric model of the simulation was extracted from the SEM test results, and the simulation results of the final breakdown path are shown in Figure 8; the calculation formula used to simulate electrical breakdown has been provided in the support material[32]. Figure 8A1-A3 is the simulation result of pure $NaNbO_3$ ceramics. There was almost no obvious electrical tree branch phenomenon observed. With the increase of time, pure $NaNbO_3$

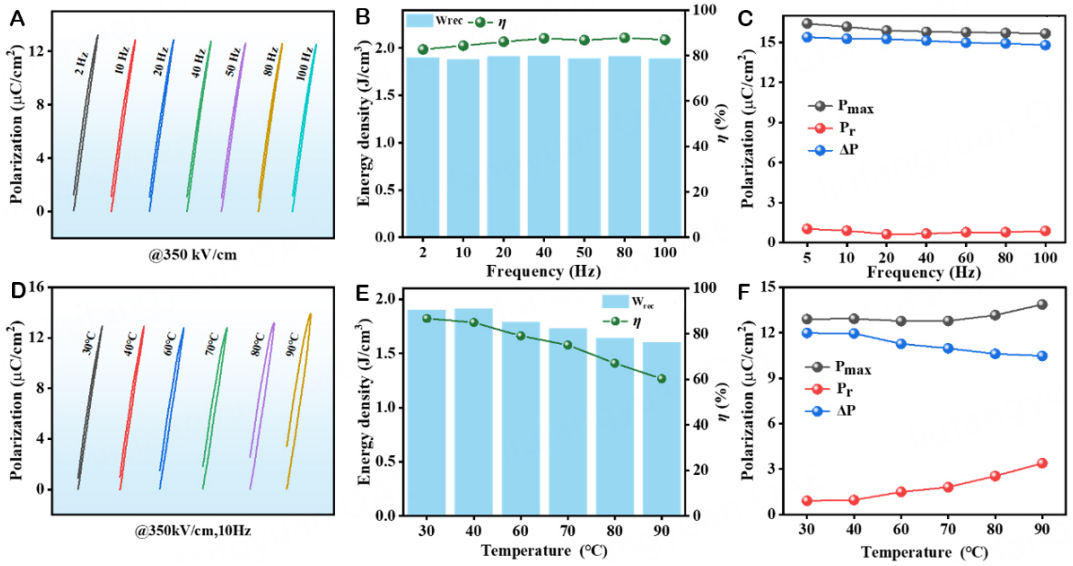

Figure 7. Unipolar P-E hysteresis loops (A and D), the corresponding energy storage properties (B and E), and P_{max}, ΔP, and P_r (C and F) for 0.08 SMZ ceramics at different frequencies and temperatures under different electric fields.

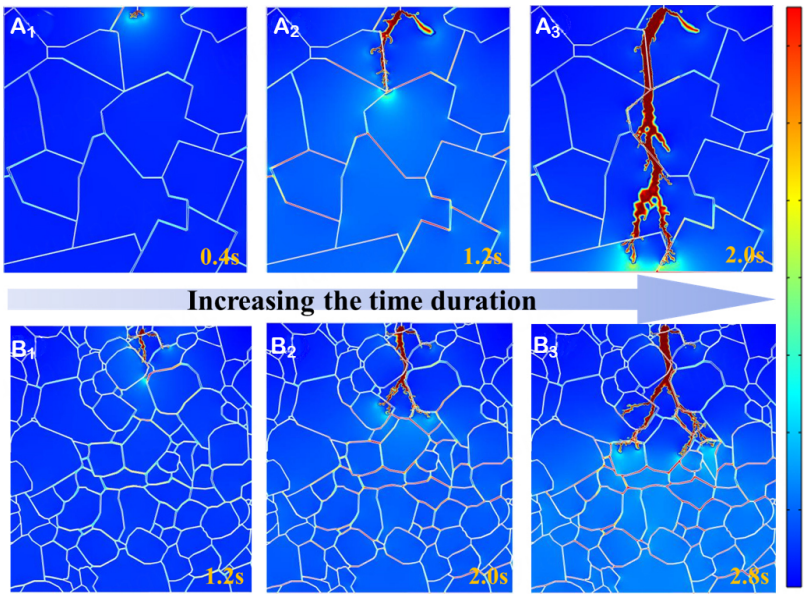

Figure 8. Breakdown paths for (1-*x*)NN-*x*SMZ samples under various times. *x* = 0: Figure 8A_1-A_3, *x* = 0.08: Figure 8B_1-B_3.

ceramics experienced a rapid electrical breakdown. The breakdown simulation of the 0.08 SMZ sample is shown in Figure 8B1-B3, and the electrical tree branch phenomenon of the sample can be clearly observed. The reason for this difference is that the average grain sizes of 0.08 SMZ ceramics were much smaller than those of pure $NaNbO_3$ ceramics. The smaller grain sizes were beneficial to generate more energy dissipation regions to suppress the breakdown behavior, which was manifested as the phenomenon of electrical tree branches. Usually, the more branches indicated that the material was more difficult to be broken down, which can also be proved by the marking time.

To understand further the intrinsic reason for the high E_b of the doped SMZ sample, impedance tests were conducted on the NN-SMZ sample. Because the impedance test pattern curve was semicircular and there was almost no difference between the grain boundary and the grain response, a set of RQC structures was used to fit the resistance of the NN-SMZ sample[33,34]. The test and fitting results are shown in Figure 9A-D. In Supplementary Figure 5, the curve of the imaginary part changing with frequency has only a single peak, which also proves this point. Supplementary Figure 6 shows the relationship between the AC conductivity of the NN-SMZ sample and the frequency change. The incorporation of SMZ reduced the conductivity of the sample, which was beneficial for obtaining a higher breakdown field strength.

Figure 9E shows that under the test condition of 560 °C, the resistance of the sample increased gradually with the incorporation of SMZ. When x = 0.15, the resistance of the sample reached a maximum value of 70,515 Ω. According to the activation energy calculation formula, the activation energy of each component is shown in Figure 9G. The activation energy of the sample increases with increasing SMZ doping. In general, the higher the activation energy of the sample, the larger its energy barrier, the more energy it needs to break down, and the higher its breakdown field strength[34,35]. To study the bandgap of the NN-SMZ ceramics further, ultraviolet test results of the samples are shown in Figure 9F. The Tauc equation was used to estimate the E_g value[36]. The E_g values of the NN-SMZ samples were 3.31, 3.37, 3.42, and 3.45 eV, which also indicated that the bandgap of the samples gradually increased[37]. This may have been caused by the incorporation of Sm_2O_3 and ZrO_2, which had large bandgaps. In summary, due to its significantly smaller grain size, the NN-SMZ sample obtained a higher breakdown field strength than the pure NN sample. Although the average grain sizes of each component increased with the increase of SMZ doping amount, the resistance and conductivity of each component increased. In terms of intrinsic factors, the band gap of the sample was increased, which helped the sample to obtain a high E_b.

The charge-discharge test of the sample was helpful for exploring its actual energy storage capacity. The data for the NN-SMZ samples under different electric fields at room temperature are shown in Figure 10A and B. In the environment of 2-18 kV, the I_{max} of the sample gradually increased to 54.9 A, the current density of the sample increased from 172.7 A/cm^2 to 777.1 A/cm^2, and the power density of the sample increased to 69.93 MW/cm^3[35,38]. The charge-discharge test of samples was performed in the range of 30 °C-100 °C under a field strength of 16 kV/mm. The results are shown in Supplementary Figure 7. The I_{max} value of the sample was 48.93 ± 3 A, the current power was 692 ± 40 A/cm^2, and the change rate of the test results was within 5%, indicating that NN-SMZ can maintain stable performance under working environments with different temperatures[38,39].

To judge the feasibility of the practical application of the NN-SMZ ceramics, a 210-Ω resistor was connected to perform an overdamped charge-discharge test on the sample. As shown in Figure 10C and D and Supplementary Figure 8A, when the applied electric field of the 0.08 SMZ sample gradually increased to 18 kV/cm at 30 °C, the current increased to 11.5 A, the discharge energy density W_d increased to 0.33 J/cm^3, and an ultrafast stable discharge time ($t_{0.9}$) of 57 ± 5 ns was obtained. As shown in Supplementary Figure 8B-D, when the temperature of the 0.08 SMZ sample increased from 30 °C to 100 °C under the condition of 16 kV/cm, the current remained at a stable value of 10.185 A ± 1%, and the value of $t_{0.9}$ was stable at 55 ± 3 ns. This shows that 0.08 SMZ can maintain stable performance under working conditions with different temperatures and meet the needs of actual pulse capacitors[40-42].

CONCLUSION

In this study, NN-SMZ was prepared by solid-phase sintering. The crystal phase of NN-SMZ gradually changed from the orthorhombic phase (*Pnma*) to the pseudocubic phase (*Pm3m*) with increasing SMZ

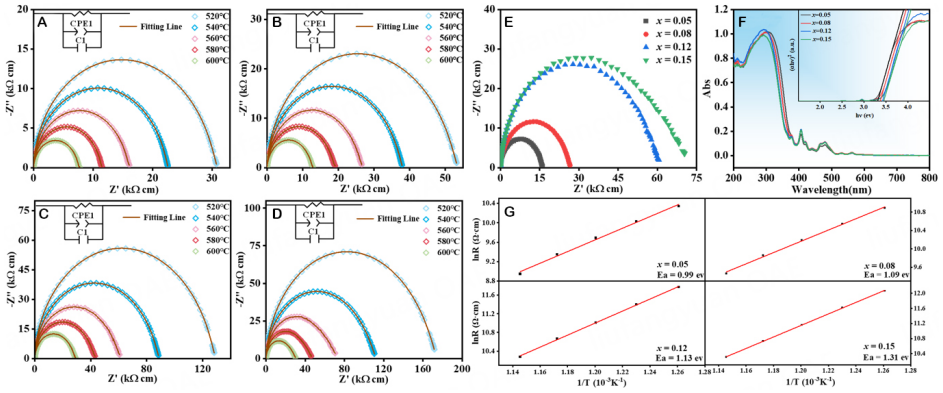

Figure 9. Impedance diagram of NN-SMZ ceramics. (A) x = 0.05, (B) x = 0.08, (C) x = 0.12, and (D) x = 0.15. (E) Impedance diagram of NN-SMZ components at 560 °C, (F) Band gap energy for NN-SMZ ceramics, (G) The fitted activation energy of NN-SMZ.

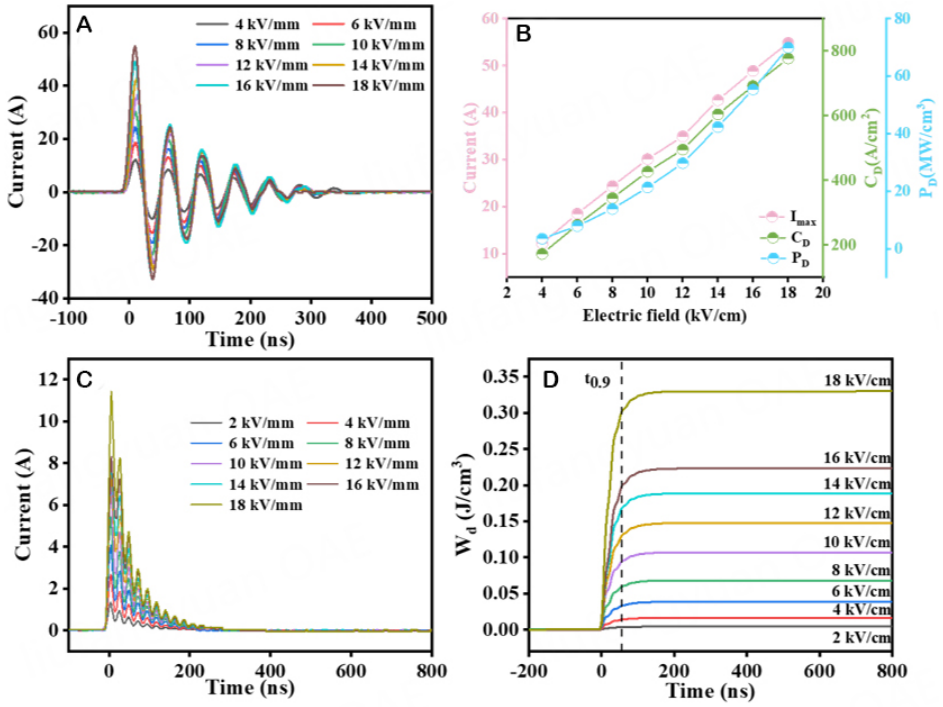

Figure 10. (A) Underdamped discharge waveform of 0.08 SMZ ceramics at room temperature. (B) The changes of I_{max}, C_D, and P_D at room temperature. (C) Over-damped discharge current curves of 0.08 SMZ ceramics at different temperatures. (D) The changes of I_{max}, C_D, and P_D under different conditions.

doping. Meanwhile, an increase in the SMZ significantly reduced the residual polarization intensity of the system and improved the breakdown field strength, resistance, and activation energy of the system. In addition, $0.92NaNbO_3$-0.08 SMZ achieved a 4.3 J/cm³ energy storage density and 85.6% energy storage efficiency at 560 kV/cm. Finally, the 0.08 SMZ ceramics showed excellent dielectric stability in charge and discharge tests, indicating their potential for practical applications. In summary, rare-earth-based composite perovskites can be used to optimize the energy storage performance of $NaNbO_3$ ceramics.

DECLARATIONS

Authors' contributions

Writing original draft, Writing review and editing: Xu M
Conceptualization : Xu M, Zhou H, Chen X
Methodology: Xu M
Investigation and data curation: Xu M, Zeng D, Wang X, Nong P, Pan Y, Dong Q, Wang J
Supervision, project administration and funding acquisition: Zhou H, Chen X

Availability of data and materials

Not applicable.

Financial support and sponsorship

This work was supported by the Natural Science Foundation of China (No. 12064007, No. 11664008 and No. 61761015), Natural Science Foundation of Guangxi (No. 2018GXNSFFA050001, No. 2017GXNSFDA198027, and No. 2017GXNSFFA198011), and High-Level Innovation Team and Outstanding Scholar Program of Guangxi Institutes.

Conflicts of interest

All authors declared that there are no conflicts of interest.

Ethical approval and consent to participate

Not applicable.

Consent for publication

Not applicable.

REFERENCES

1. Wang X, Dong Q, Pan Y, et al. Enhanced energy storage performances of $Bi(Ni_{1/2}Sb_{2/3})O_3$ added $NaNbO_3$ relaxor ferroelectric ceramics. *Ceram Int* 2022;48:13862-8. DOI
2. Wang W, Zhang L, Shi W, et al. Enhanced energy storage properties in lead-free $(Na_{0.5}Bi_{0.5})_{0.7}Sr_{0.3}TiO_3$-based relaxor ferroelectric ceramics through a cooperative optimization strategy. *ACS Appl Mater Interfaces* 2023;15:6990-7001. DOI
3. Pan Y, Wang X, Dong Q, et al. Enhanced energy storage properties of $Bi(Ni_{2/3}Nb_{1/6}Ta_{1/6})O_3$-$NaNbO_3$ solid solution lead-free ceramics. *Ceram Int* 2022;48:26466-75. DOI
4. Dong Q, Wang X, Wang J, et al. Enhanced energy storage performance in $Na_{(1-3x)}BixNb_{0.85}Ta_{0.15}O_3$ relaxor ferroelectric ceramics. *Ceram Int* 2022;48:776-83. DOI
5. Xie A, Qi H, Zuo R, Tian A, Chen J, Zhang S. An environmentally-benign $NaNbO_3$ based perovskite antiferroelectric alternative to traditional lead-based counterparts. *J Mater Chem C* 2019;7:15153-61. DOI
6. Xie A, Zuo R, Qiao Z, Fu Z, Hu T, Fei L. $NaNbO_3$-$(Bi_{0.5}Li_{0.5})TiO_3$ lead-free relaxor ferroelectric capacitors with superior energy-storage performances via multiple synergistic design. *Adv Energy Mater* 2021;11:2101378. DOI
7. Chen H, Chen X, Shi J, et al. Achieving ultrahigh energy storage density in $NaNbO_3$-$Bi(Ni_{0.5}Zr_{0.5})O_3$ solid solution by enhancing the breakdown electric field. *Ceram Int* 2020;46:28407-13. DOI
8. Ye J, Wang G, Chen X, Dong X. Effect of rare-earth doping on the dielectric property and polarization behavior of antiferroelectric sodium niobate-based ceramics. *J Mater* 2021;7:339-46. DOI
9. Chen J, Si F, Zhao P, Zhang S, Tang B. Novel lead-free $(1-x)Sr_{0.7}Bi_{0.2}TiO_{3-x}La(Mg_{0.5}Zr_{0.5})O_3$ energy storage ceramics with high charge-discharge and excellent temperature-stable dielectric properties. *Ceram Int* 2021;47:26215-23. DOI
10. Yang L, Qi J, Yang M, et al. High comprehensive energy storage properties in (Sm, Ti) co-doped sodium niobate ceramics. *Appl Phys Lett* 2023;122:192901. DOI
11. Qu N, Du H, Hao X. A new strategy to realize high comprehensive energy storage properties in lead-free bulk ceramics. *J Mater Chem C* 2019;7:7993-8002. DOI

12. Yuan Q, Li G, Yao F, et al. Simultaneously achieved temperature-insensitive high energy density and efficiency in domain engineered $BaTiO_3$-$Bi(Mg_{0.5}Zr_{0.5})O_3$ lead-free relaxor ferroelectrics. *Nano Energy* 2018;52:203-10. DOI
13. Zeng D, Dong Q, Nong P, et al. Achieving high energy storage density in $BaTiO_3$- $(Bi_{0.5}Li_{0.5})(Ti_{0.5}Sn_{0.5})O_3$ lead-free relaxor ferroelectric ceramics. *J Alloys Compd* 2023;937:168455. DOI
14. Dong X, Li X, Chen H, et al. Realizing enhanced energy storage and hardness performances in $0.90NaNbO_3$-$0.10Bi(Zn_{0.5}Sn_{0.5})O_3$ ceramics. *J Adv Ceram* 2022;11:729-41. DOI
15. Shannon RD. Revised effective ionic radii and systematic studies of interatomic distances in halides and chalcogenides. *Acta Cryst A* 1976;32:751-67. DOI
16. Hreščak J, Dražić G, Deluca M, et al. Donor doping of $K_{0.5}Na_{0.5}NbO_3$ ceramics with strontium and its implications to grain size, phase composition and crystal structure. *J Eur Ceram Soc* 2017;37:2073-82. DOI
17. Schulz T, Veerapandiyan VK, Gindel T, Deluca M, Töpfer J. Hexavalent (*Me* - W/Mo)-modified $(Ba,Ca)TiO_3$-$Bi(Mg,Me)O_3$ perovskites for high-temperature dielectrics. *J Am Ceram Soc* 2020;103:6881-92. DOI
18. Chen H, Wang X, Dong X, et al. Adjusting the energy-storage characteristics of $0.95NaNbO_3$-$0.05Bi(Mg_{0.5}Sn_{0.5})O_3$ ceramics by doping linear perovskite materials. *ACS Appl Mater Interfaces* 2022;14:25609-19. DOI
19. Shi J, Chen X, Sun C, et al. Superior thermal and frequency stability and decent fatigue endurance of high energy storage properties in $NaNbO_3$-based lead-free ceramics. *Ceram Int* 2020;46:25731-7. DOI
20. Xie A, Qi H, Zuo R. Achieving remarkable amplification of energy-storage density in two-step sintered $NaNbO_3$-$SrTiO_3$ antiferroelectric capacitors through dual adjustment of local heterogeneity and grain scale. *ACS Appl Mater Interfaces* 2020;12:19467-75. DOI PubMed
21. Dai Z, Xie J, Fan X, et al. Enhanced energy storage properties and stability of $Sr(Sc_{0.5}Nb_{0.5})O_3$ modified $0.65BaTiO_3$-$0.35Bi_{0.5}Na_{0.5}TiO_3$ ceramics. *Chem Eng J* 2020;397:125520. DOI
22. Wang H, Yuan H, Li X, et al. Enhanced energy density and discharged efficiency of lead-free relaxor $(1-x)[(Bi_{0.5}Na_{0.5})_{0.94}Ba_{0.06}]_{0.98}La_{0.02}TiO_{3-x}KNb_{0.6}Ta_{0.4}O_3$ ceramic capacitors. *Chem Eng J* 2020;394:124879. DOI
23. Li X, Xing J, Wang F, et al. Realizing high energy density and efficiency simultaneously in $(Bi_{0.5}Na_{0.5})_{0.7}Sr_{0.3}TiO_3$-based ceramics *via* introducing linear dielectric $CaTiO_3$. *J Mater Chem A* 2022;10:18343-53. DOI
24. Liu G, Chen L, Qi H. Energy storage properties of $NaNbO_3$-based lead-free superparaelectrics with large antiferrodistortion. *Microstructures* 2023;3:2023009. DOI
25. Xie A, Chen J, Zuo J, et al. Excellent energy-storage performance of $(0.85 - x)NaNbO_3$-$xNaSbO_3$-$0.15(Na_{0.5}La_{0.5})TiO_3$ antiferroelectric ceramics through B-site Sb^{5+} driven phase transition. *ACS Appl Mater Interfaces* 2023;15:22301-9. DOI
26. Pang F, Chen X, Shi J, et al. $Bi(Mg_{0.5}Sn_{0.5})O_3$-doped $NaNbO_3$ lead-free ceramics achieve excellent energy-storage and charge/discharge performances. *ACS Sustain Chem Eng* 2021;9:4863-71. DOI
27. Ding Y, Li P, He J, et al. Simultaneously achieving high energy-storage efficiency and density in Bi-modified $SrTiO_3$-based relaxor ferroelectrics by ion selective engineering. *Compos B Eng* 2022;230:109493. DOI
28. Zhou M, Liang R, Zhou Z, Dong X. Novel $BaTiO_3$-based lead-free ceramic capacitors featuring high energy storage density, high power density, and excellent stability. *J Mater Chem C* 2018;6:8528-37. DOI
29. Yadav AK, Fan H, Yan B, et al. High strain and high energy density of lead-free $(Bi_{0.50}Na_{0.40}K_{0.10})_{0.94}Ba_{0.06}Ti_{(1-x)}(Al_{0.50}Ta_{0.50})_xO_3$ perovskite ceramics. *J Mater Sci* 2020;55:11137-50. DOI
30. Li T, Chen P, Li F, Wang C. Energy storage performance of $Na_{0.5}Bi_{0.5}TiO_3$-$SrTiO_3$ lead-free relaxors modified by $AgNb_{0.85}Ta_{0.15}O_3$. *Chem Eng J* 2021;406:127151. DOI
31. Li X, Tan Z, Xing J, et al. Simultaneous enhancement of energy storage and hardness performances in $(Na_{0.5}Bi_{0.5})_{0.7}Sr_{0.3}TiO_3$-based relaxor ferroelectrics *via* multiscale regulation. *ACS Appl Mater Interfaces* 2022;14:42245-57. DOI
32. Cai Z, Wang X, Hong W, Luo B, Zhao Q, Li L. Grain-size-dependent dielectric properties in nanograin ferroelectrics. *J Am Ceram Soc* 2018;101:5487-96. DOI
33. Li F, Zhai J, Shen B, Zeng H, Jian X, Lu S. Multifunctionality of lead-free $BiFeO_3$-based ergodic relaxor ferroelectric ceramics: high energy storage performance and electrocaloric effect. *J Alloys Compd* 2019;803:185-92. DOI
34. Zhao N, Fan H, Li C, Huang F, Cao J, Li Z. Enhanced energy storage density and efficiency in Sm^{3+}-doped $((Bi_{0.5}Na_{0.5})_{0.7}(Sr_{0.7}Bi_{0.2})_{0.3}))TiO_3$ ceramics. *J Mater Sci Mater Electron* 2021;32:24930-8. DOI
35. Zhang M, Yang H, Li D, Lin Y. Excellent energy density and power density achieved in $K_{0.5}Na_{0.5}NbO_3$-based ceramics with high optical transparency. *J Alloys Compd* 2020;829:154565. DOI
36. Pu Y, Wang W, Guo X, Shi R, Yang M, Li J. Enhancing the energy storage properties of $Ca_{0.5}Sr_{0.5}TiO_3$-based lead-free linear dielectric ceramics with excellent stability through regulating grain boundary defects. *J Mater Chem C* 2019;7:14384-93. DOI
37. Dong X, Li X, Chen X, Wu J, Zhou H. Simultaneous enhancement of polarization and breakdown strength in lead-free $BaTiO_3$-based ceramics. *Chem Eng J* 2021;409:128231. DOI
38. Tian A, Zuo R, Qi H, Shi M. Large energy-storage density in transition-metal oxide modified $NaNbO_3$-$Bi(Mg_{0.5}Ti_{0.5})O_3$ lead-free ceramics through regulating the antiferroelectric phase structure. *J Mater Chem A* 2020;8:8352-9. DOI
39. Muhammad R, Ali A, Camargo J, et al. Enhanced thermal stability in dielectric properties of $NaNbO_3$-modified $BaTiO_3$-$BiMg_{1/2}Ti_{1/2}O_3$ ceramics for X9R-MLCC applications. *Crystals* 2022;12:141. DOI
40. Xu M, Wang X, Nong P, et al. $0.90(0.88NaNbO_3$-$0.12Bi(Ni_{0.5}Zr_{0.5})O_3)$-$0.10CaTiO_3$ lead-free dielectric ceramics with high energy storage properties. *ACS Appl Energy Mater* 2023;6:1630-8. DOI

41. Li X, Cheng Y, Wang F, et al. Enhancement of energy storage and hardness of $(Na_{0.5}Bi_{0.5})_{0.7}Sr_{0.3}TiO_3$-based relaxor ferroelectrics *via* introducing $Ba(Mg_{1/3}Nb_{2/3})O_3$. *Chem Eng J* 2022;431:133441. DOI
42. Lin Y, Li D, Zhang M, Yang H. $(Na_{0.5}Bi_{0.5})_{0.7}Sr_{0.3}TiO_3$ modified by $Bi(Mg_{2/3}Nb_{1/3})O_3$ ceramics with high energy-storage properties and an ultrafast discharge rate. *J Mater Chem C* 2020;8:2258-64. DOI